# Measurements of Radiation Heat Flux to a Probe Surface in the NASA Ames IHF Arc Jet Facility

Michael W. Winter<sup>1</sup>
University Affiliated Research Center, UC Santa Cruz, NASA Ames Research Center, Moffett Field, CA 94035

George A. Raiche, <sup>2</sup> Imelda Terrazas-Salinas, <sup>3</sup> Frank C. L. Hui<sup>4</sup>, Bruce White <sup>5</sup> NASA Ames Research Center, Moffett Field, CA 94035

Jaswinder S. Taunk<sup>6</sup>, *Jacobs Technology NASA Ames Research Center, Moffett Field, CA 94035* 

An optical probe was applied to measure radiation from inside the arc heater incident on a test sample immersed in the arc-heated stream through spectroscopy and radiometry. Unlike efforts of the past, where the probe line of sight was inclined to the nozzle centerline, the present development focused on having the probe line of sight coincide with the nozzle centerline. A fiber-coupled spectrometer was used to measure the spectral distribution of incident radiation in the wavelength range of 250 to 950 nm. The radiation heat flux in this wavelength range was determined by integration of the measured spectral intensity calibrated to incident irradiance from an integrating sphere. In addition, total radiation measurements were made with thermopile sensors. Due to the flat spectral characteristics of these sensors, the detected wavelength range was only limited by the sapphire windows which typically cut off radiation below 160nm and above ~5µm. Several arc-heater conditions, corresponding to stream bulk enthalpy levels between 8 and 24 MJ/kg, were investigated in the 6-inch diameter nozzle of the Interaction Heating Facility at NASA Ames Research Center. The results are compared to former measurements with the 13-inch diameter nozzle. With the probe placed at a distance of 3 inches from the nozzle exit plane, total radiative heat fluxes were measured to be between 8 and 33 W/cm<sup>2</sup> for the different conditions. In correspondence with the measurements in the 13-inch nozzle, the spectra are dominated by continuum emission. However, with the 6-inch nozzle, the ratios of boundbound to continuum are observed to be higher. The factors between measurements with the 6-inch and the 13-inch nozzle yield the conclusion that for the highest condition, without added cold air, the majority of the measured bound-bound radiation is generated in the cathode region of the arc heater. The measured continuum radiation, however, seems to be generated mainly close to the upstream electrode in the first part of the arc-column. For the condition with significant add air, the radiation heat flux increase is almost the same for bound-bound and continuum radiation. If the arc-column distribution is considered to remain unchanged, this indicates additional continuum radiation to be generated close to the downstream electrode and bound-bound emission in the downstream region to be reduced. These effects are attributed to the added room temperature air at this condition. In the tested configuration with the 6-inch nozzle, the measured radiative heat flux accounts for up to 1.5% of the total heat flux on a hemispheric calorimeter or 2.7% on a flat face. Although stronger than anticipated, these values can still be considered negligible as a heat load.

<sup>&</sup>lt;sup>1</sup> Research Scientist, Aerothermodynamics Branch, M/S 230-3, Senior Member AIAA.

<sup>&</sup>lt;sup>2</sup> Branch Chief Thermo-Physics Facilities Branch, MS 229-2. Member AIAA

<sup>&</sup>lt;sup>3</sup> Lead Test Engineer, Thermo-Physics Facilities Branch, MS 229-4

<sup>&</sup>lt;sup>4</sup> Test Engineer, Thermo-Physics Facilities Branch, MS 229-4. Member AIAA

<sup>&</sup>lt;sup>5</sup> Electrical Engineer, Engineering Systems Division, MS 213-2, no AIAA Member

<sup>&</sup>lt;sup>6</sup> Senior Research Engineer, Thermo-Physics Facilities Branch, MS 229-4, AIAA member.

#### I. Introduction

THE development and qualification of heatshield materials for high-speed atmospheric entries relies heavily on ground testing in high enthalpy plasma facilities such as the arc jets at NASA Ames Research Center (ARC). One of the key parameters for material testing is the heat flux to a material sample. Calorimeter measurements are used to determine the heat flux characteristic for the chosen test conditions. So far, the heat flux to a surface is assumed to be solely determined by the properties of the plasma forming behind the bow shock in front of the material sample. A high-temperature plasma, however, emits a significant amount of radiation and constricted arc heaters produce an extended plasma volume at high temperature and pressure inside the heater. The plasma radiation will hit the surface of a probe or a material sample in the plasma beam and contribute to the heating. The effect of radiative heating will be different on a metallic heat flux probe and a material sample due to the different absorption coefficients, therefore biasing the heat flux measurements. In consequence, the material sample will typically "see" a higher heat flux than the metallic calorimeter. The goal of this work is to measure this radiative heating and quantify its contribution during arc-jet testing.

The 60 MW Interaction Heating Facility (IHF), one of several arc jet facilities at NASA Ames Research Center, is used to test and qualify spacecraft thermal protection materials in "flight-like" aerothermal environments. The IHF heater is a constricted arc design with an upstream anode, and a downstream cathode, which consists of 8 electrode disks. The working gas is injected along the arc-column. The discharge is established between the anode and the cathode, and the working gas is heated to temperatures of 8000 K or more. The magnitude of these temperatures, hence the flow energy, depend on the input current, voltage, and flow rates. Following the cathode, there are 4 disks/segments through which additional room temperature air can be injected to tailor the enthalpy of the working medium to the desired test value. This set of 4 segments is referred to as the "plenum" in the present work. The working gas, of appropriate enthalpy, is then expanded into the test chamber through a convergent-divergent nozzle, and the test article is placed in the free jet. Different nozzle geometries, mainly defined by the nozzle exit diameter, can be used to obtain various heat fluxes and pressures on a material sample. For this work, nozzle exit diameters of 6" and 13" are used. Figure 1 shows a sketch of the IHF design.

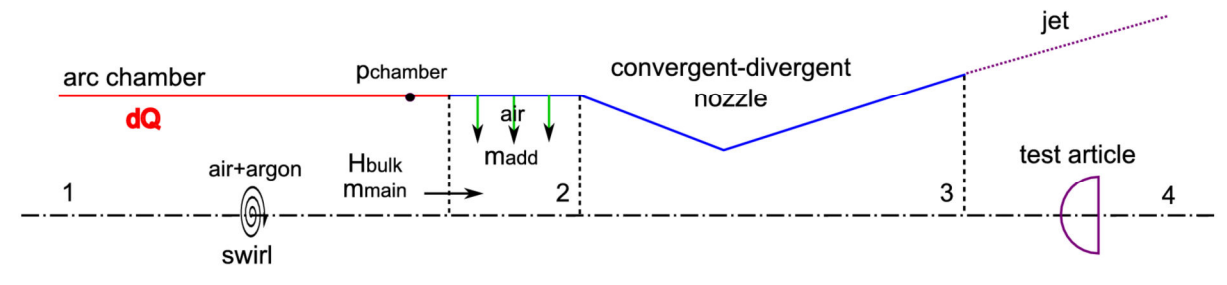


Figure 1. Sketch of the IHF working principle.

Over the last two years measurement campaigns involving optical emission spectroscopy for the characterization of re-entry plasmas in the Ames arc-jet facilities have been conducted. These measurement campaigns focused on the plenum<sup>1</sup> of the IHF arc-heater and the free jet<sup>2</sup> in the test chamber to support facility characterization and provide validation data for CFD simulations. Both equilibrium conditions in the plenum and non-equilibrium effects in the free stream were discussed in the work of Winter  $et\ al.^{1,\ 2}$ 

Recently, an optical probe was designed to measure incident radiation on a sample in the arc-jet flow to quantify the radiative loads by measurements. Prior to this work, there were only estimates available for the radiation from the inside of the heater impinging on a material sample or probe surface. In a first attempt, the impinging radiation was measured spectrally resolved with a fiber coupled spectrometer with the 13-inch nozzle configuration.<sup>3</sup> The radiation heat fluxes were found to account for 1.4% of the total heat flux to a flat face calorimeter and thus are considered negligible. However, high heat flux and high pressure requirements often favor measurements with the 6-inch nozzle configuration. The condition inside the arc heater is not supposed to change through the nozzle since the supersonic expansion does not allow communication in the upstream direction. The distance to the radiating plasma, however, decreases significantly and radiation heat fluxes will increase by switching from the 13-inch nozzle to the 6-inch one. Initial estimates of this increase were made after the measurements with the 13-inch configuration, however, the assumptions required for this analysis prevented a conclusive prognosis. Therefore, the measurements were repeated with the 6-inch nozzle configuration and total radiation measurements with thermopile radiometers were added.

## II. Measurement Strategy and Instrumentation

The test strategy for the spectroscopy measurements to sweep the optical probe through the free jet (Fig. 2) with a defined sweep velocity was adopted from the measurement campaign with the 13-inch nozzle.<sup>3</sup> During the sweep time the spectrometer continuously acquired data and stored them in the local (on-board) memory. Maximum data acquisition speeds are on the order of 250 Hz with minimum acquisition times of 1.1µs for each individual spectrum. The data acquisition of the spectrometer was triggered by a 5 V TTL (Transistor-Transistor Logic) pulse once the probe was set into motion. Both trigger and position readings of the sting arm were stored in the facility data acquisition system to enable synchronization with the spectra stored in the internal memory of the spectrometer. Figure 2 illustrates the measurement strategy showing three probe positions during the sweep, firstly with the probe outside the flow, then looking at the nozzle wall with a shock already building up, and finally at the center line measuring the sum of plenum and post-shock emission. In previous measurements,<sup>3</sup> it was shown that the contribution of the post shock radiation can be neglected in the given probe configuration.

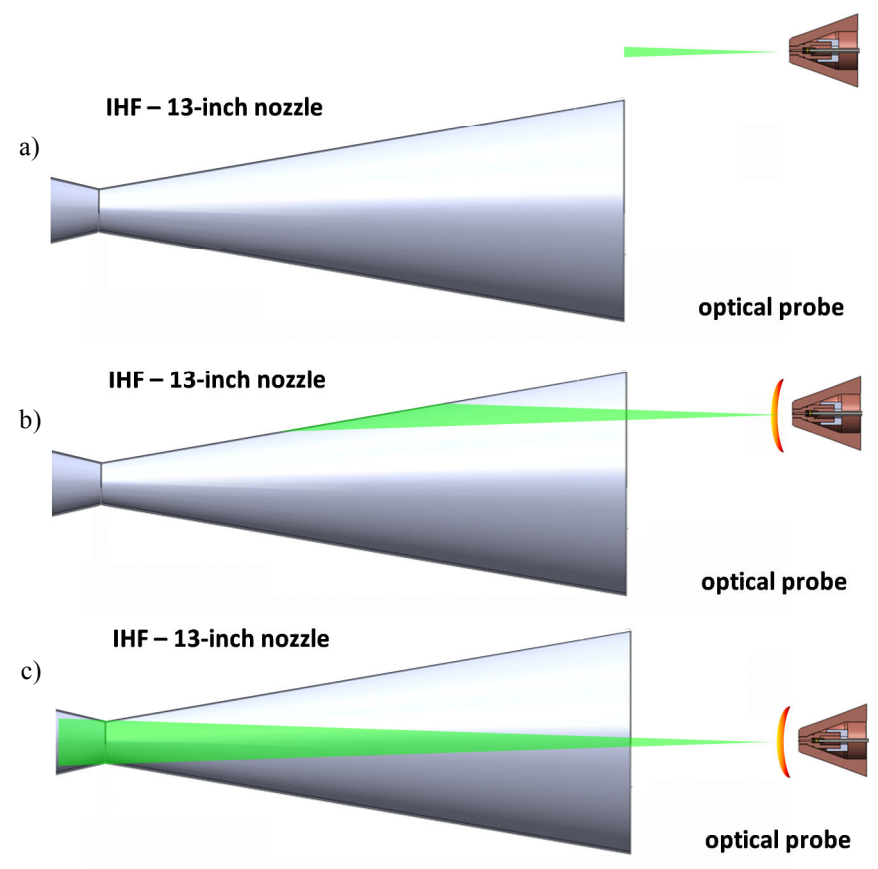


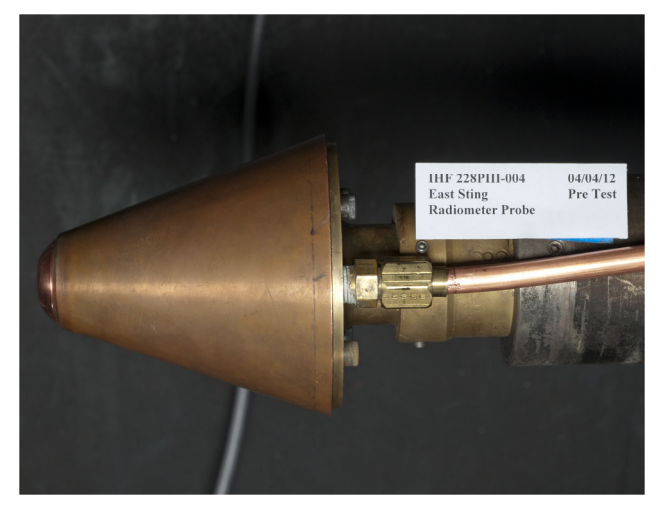
Figure 2. Measurement strategy during Optical Probe sweep through the plasma flow of the IHF arc-jet. a) Optical probe outside the plasma flow, b) probe "seeing' the cold wall, and c) at the center line.

The optical signals were collected through a combination of two optical fibers of 2.5m length which were routed to an optical table outside the test chamber through a vacuum duct and connected to an Ocean Optics filter coupler. Two different neutral density filters (T0.007 and ND4 with nominal transmittances of 0.7% and 0.01%) were used to further reduce the signal strength. The filter holder was coupled through one more fiber of 1m length to the spectrometer (Avantes AvaSpec-3648-USB2-UA, nominal wavelength range 180-1100nm). In configuration used, the useful wavelength range was 250-950nm with a full width at half maximum (FWHM) of about 1.3nm. Acquisition times during arc-jet testing varied between 10µs and 4ms.

In addition to the spectrometer probe, a radiometer was placed in a second cone on a different string arm to provide total radiation measurements during the same arc-jet run.

Due to the time constant of the sensor of about 60ms to reach 67% of the final signal, these measurements were conducted through an insertion of this probe with times on the center line between 0.5 and 1 second.

In parallel to the optical probe measurements, plenum spectroscopy similar to prior measurement campaigns<sup>1</sup> was conducted to obtain additional information about the plasma condition prior to its expansion in the nozzle. The optical measurements were accompanied by single-point center line heat flux and pressure measurements with a 102-mm-diameter hemispherical copper slug calorimeter. Figure 3 shows photos of the optical probe mounted on the IHF sting arm and during the arc-jet test at the nozzle center line.



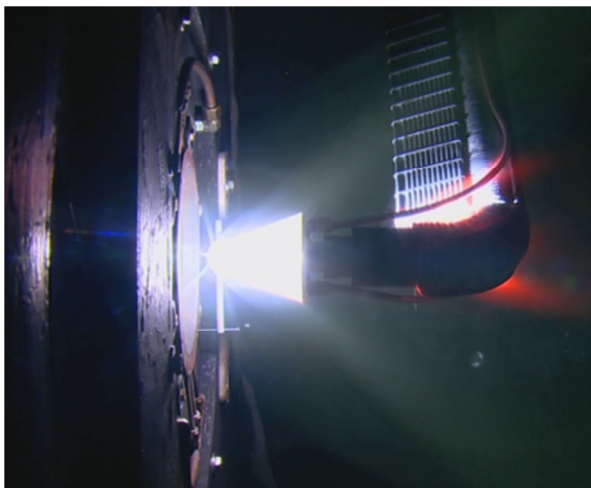


Figure 3. Optical probe mounted on the IHF sting arm and during testing with the IHF 6 inch nozzle.

## III. Probe Design and Alignment

The probe design is based on a water-cooled probe body that carries an optical plug with a sapphire window to seal the optical path against the post shock plasma and a mechanical connection for an optical fiber. The design from previous test campaigns had to be modified to provide a sufficient field of view to cover all radiation emitted from inside the arc heater. On the arc-jet side, the limiting aperture is the nozzle throat, which defines the necessary field of view. On the probe side, the front mask is the limiting aperture stop. The probe cones were initially designed to be used behind a material sample set-up. Therefore, an additional copper front cap was used to protect the front surface of the probe body itself (which actually melted at two conditions). At the highest enthalpy condition in the 6-inch nozzle configuration, even this copper cap was not sufficient to protect the water-cooled probe body which finally showed water leaks after this test. Therefore, a thoroughly water cooled probe body, preferably in a hemispherical shape is recommended for future test campaigns.

The optical path is limited through aperture stops only, without focusing elements. Thus, each point in the field of view sees, in good approximation, the same receiving surface (the fiber aperture or the radiometer pinhole) which corresponds to very similar solid angles in which radiation is emitted. The sensitivity is almost constant across the field of view.<sup>3</sup> However, the coupling into the fiber under different angles might cause slight variations in sensitivity of the spectrometer set-up. The necessary field of view for testing in the IHF equipped with the 6'' nozzle is defined by the nozzle throat diameter, which is the limiting aperture stop for radiation coming from the inside of the heater. At a probe position of 3 inches from the nozzle exit, the half-angle of the necessary field of view becomes  $4.4^{\circ}$  which is also the maximum angle under which radiation has to be fed into the fiber or to the thermopile sensor. This value is clearly smaller than the critical acceptance angle of the optical fiber of  $\pm 12.7^{\circ}$ , as defined by its numerical aperture of 0.22. For the thermopile, the distance between the pinhole and the sensing area was adapted accordingly to account for this opening angle.

# **Spectrometer Probe Design**

The spectrometer was located outside the arc-jet test box and the optical signals were fed to the spectrometer by optical fibers. The use of optical plugs from the plenum spectroscopy development had to be abandoned due to geometry restrictions with the required half opening angle of at least  $\pm 4.4$  deg to the nozzle throat. Instead, the sapphire window, the sealing O-ring, and the SMA connector were directly incorporated in the optical plug which was screwed into the probe body. This unit still can be mounted in the optical path as an entire entity.

The rear plug and the front cap are threaded into the water-cooled probe body. The rear plug is mounted from the back of the probe before mounting it on the sting arm and carries the aforementioned optics and the connector to the optical fiber. The front plug can be inserted and taken out while the probe is mounted and aligned. Therefore, different entrance apertures can be used without changing the alignment. Figure 4 shows the third generation design for optical fibers connected to a spectrometer.

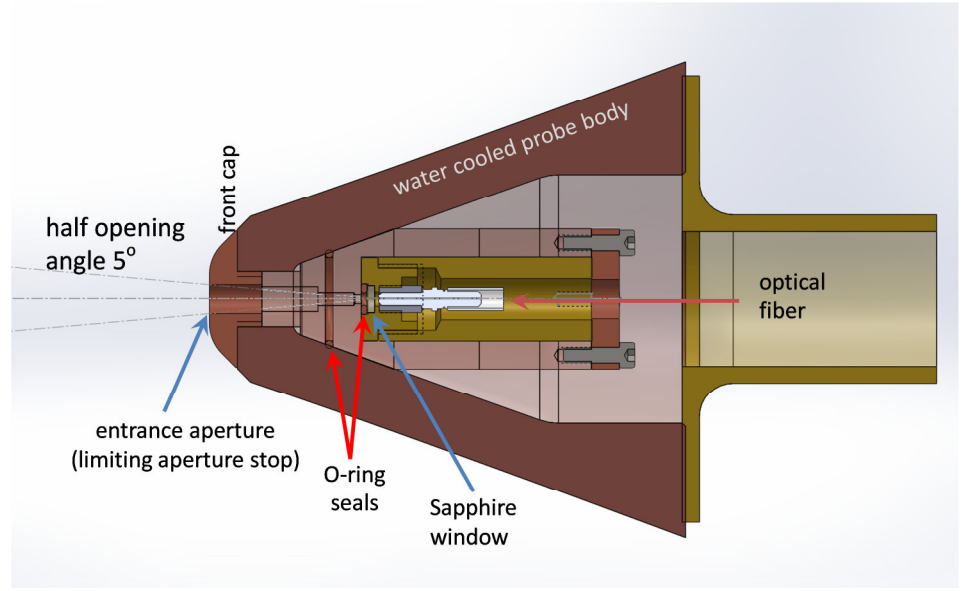


Figure 4. Third generation spectrometer probe design without focusing element.

## **Radiometer Probe Design**

The radiometer design contains an aperture stop limited optical path, sensor element and sensor electronics inside the sting arm. As sensing element, a Dexter Research ST-120 temperature compensated thermopile was used. Temperature compensation is achieved through a second thermopile sensor which is shielded from the radiation and therefore experiences environmental changes (i.e. usually temperature changes of the whole sensor) the same way as the radiation sensing thermopile and can be used to compensate for these changes. An extrapolation of radiation fluxes from previous measurements lead to radiation levels of up to 70 W/cm². The sensor, however, had a destruction limit of 100 mW/cm². Therefore, a 50µm pinhole was added to the optical path, limiting the incident total radiation. The sensing area (1.2x1.2mm²) itself was placed at a defined distance to this pinhole. The optical path was chosen to blur the radiation flux on the pinhole to a value acceptable for the sensor (with completely illuminated sensor limited by the area ratio of 576). In fact, higher reduction can be achieved overfilling the sensor. However, it was decided to maintain the radiation on the pinhole, yielding slightly underfilling the sensor. Figure 5 shows the design for the radiometer sensor.

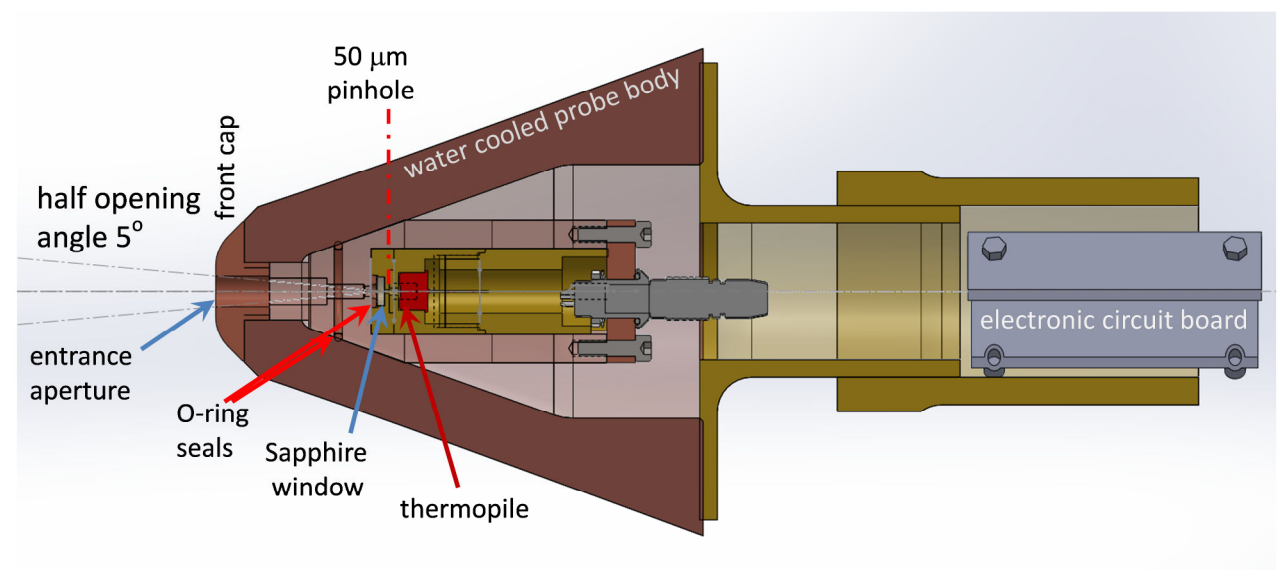


Figure 5. Radiometer probe design without focusing element.

The sensor signals were amplified by custom made electronic circuit boards as shown in Fig. 6 to transform the sensor output signals to signals detectable by the facility data acquisitions system. The two outputs of the sensor were conditioned by a two-channel instrumentation amplifier. Two versions of this amplifier were built – one with a gain of ~60 for direct measurement of plasma with an anticipated mV input range, and another with a gain of ~6000 as a calibration unit for use with a comparatively dim calibration source with an anticipated  $\mu$ V input range. Both amplifiers were further conditioned by a 2-pole active low-pass filter with a 250 Hz cutoff. Characterization of the circuits was performed with a precision  $\mu$ V/mV voltage standard to determine offset voltages and gain accuracy. The output signals of the electronic board were finally passed to the facility data acquisition system through shielded twisted paired cables. Figure 6 show the circuit board.



Figure 6. Electronic board for data acquisition during arc-jet testing.

In addition to this sensor, a window-less sensor design capable of vacuum UV measurements was investigated. On the sensor side, the ST-120 was purchased without a window and inert gas protection. On the probe side, the protective window inside the probe was also eliminated. Instead, a helium flushing concept was developed to protect the sensor from inflow of hot post-shock plasma. Helium is fed through the rear lid into the cavity which houses the sensor and cables to the sensor electronics. Two axial channels feed the helium to a groove at the front of the optical plug which connects to the center hole for optical access which has the smallest cross section in the flow path and would therefore act as a nozzle throat. Given sufficient back pressure, a sonic transition should occur at that point followed by a supersonic expansion through the increasing cross sections downstream from here. The component of the optical plugs for both radiometer designs are shown in Fig. 7.



Figure 7. Optical radiometer plug assembly for window-less set-up with helium flushing (upper) and set-up with windows (lower).

## **Probe Alignment**

For the spectrometer set-up, an alignment strategy with LEDs of different color was developed and applied in the measurement campaign with the 13-inch nozzle.<sup>3</sup> The radiometer set-up, however, was not sensitive enough to see the LEDs, therefore a different alignment strategy had to be developed to ensure the required angle accuracy of  $\pm 0.5$  deg. The alignment process contains two steps.

- 1) The facility uses a HeNe laser which is installed at the upstream end of the heater and is aligned to the center of the nozzle exit center. This laser is used to align the probe center to be on axis with the facility center line.
- 2) An alignment tool, which contains an iris at a distance of 4 inches (102 mm) to the probe surface is mounted to the probe. The probe position is adjusted to center the facility laser on the iris center. If the probe shows an angle to the facility laser, the laser dot, transmitted through the iris, will not hit the center of the probe surface in 4 inches distance. The probe center was marked by a 0.5mm rod sticking ~4mm out of the surface to assist alignment. Now, angular alignment of the probe was performed, iteratively changing the angle of the probe and readjusting its position to make sure the laser hit the iris center.

For each test, the alignment was checked with the same set-up and was found to be sufficiently stable. Figure 8 shows a picture of the alignment tool during test preparation in the IHF. In lab tests before the measurement campaign, this alignment method was checked with the spectrometer set-up versus the alignment with the LED alignment tool (which was proven to be sufficiently accurate in the former measurement campaign). The difference between the two methods was found to be negligible.

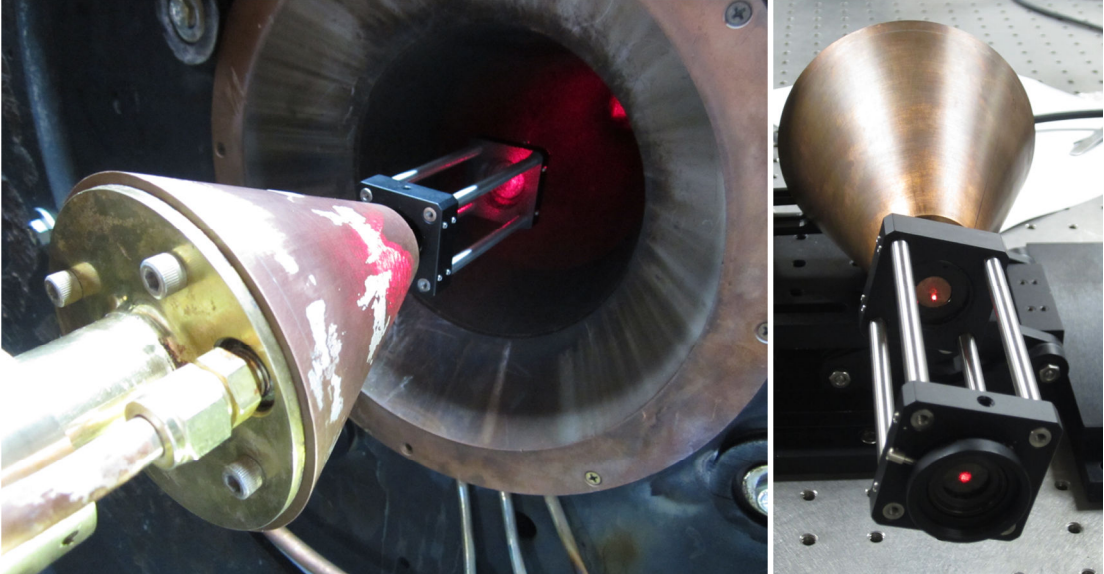


Figure 8. Laser alignment of the optical probe during IHF testing and calibration.

#### IV. Calibration

All measurements were calibrated to incident irradiance [W/cm<sup>2</sup>] through measurements of several calibration lamps (halogen bulb fed integrating spheres and a Deuterium discharge lamp) factory calibrated to spectral radiance [W/(cm<sup>2</sup> sr nm)]. The spectral radiant intensity emitted by the lamp is given as the emitted radiance multiplied by the emitting area. The receiving area  $A_{OF}$  (and therefore the solid angle from the lamp to the probe) is defined by the fiber diameter, the emitting area is defined by the opening aperture of the integrating sphere. The incident spectral irradiance I can be computed from the calibrated spectral radiance L through:

$$I(\lambda) = \frac{L(\lambda) A_{emitting} \Omega}{A_{OF}} = \frac{L(\lambda) A_{emitting}}{x_0^2}$$
(1)

 $x_0$  being the distance from the integrating sphere exit to the optical fiber entrance inside the probe body.

One particular difficulty was that the arc-jet radiation was about 4-5 orders of magnitude higher than the light provided by the calibration lamps. With the spectrometer set-up, this was compensated through the use of neutral density filters for which the spectral transmission curve could be separately determined during calibration. For the radiometer measurements, the use of such filters was not appropriate since no spectral information was available neither during actual measurements nor during calibration. Therefore, spatial filtering through a small aperture stop was used which did not alter the spectral characteristics of the sensor. At the same time, this reduction of probe sensitivity was necessary to stay below the destruction limit of the sensor itself.

## **Spectrometer Calibration**

For the spectrometer, a calibration check was done before and after each test using an integrating sphere with a distance to the probe surface of 6 inches (~152 mm) with the maximum sphere aperture of 20 mm diameter, yielding a half opening angle of about 3°, which is well within the acceptance angle of the fiber and the probe and representative for the field of view defined by the IHF nozzle throat. These measurements were performed both without any filter and with the T0.007 neutral density filter (the signals with the ND4 filter used during arc-jet testing were so weak that the required acquisition times would introduce too much noise to the measurements). Additional calibration measurements were performed after the test campaign in the optical lab with a Labsphere integrating sphere with higher power and a recent re-calibration at an appropriate distance to mirror the IHF test geometry with the sphere exit plane representing the IHF nozzle throat. However, the geometrical configuration (in particular in terms of fiber routing) was different in the lab, therefore the calibration measurements taken in between the arc-jet runs were used for the quantitative calibration and the measurements in the optical lab were only used to determine the filter transmissions.

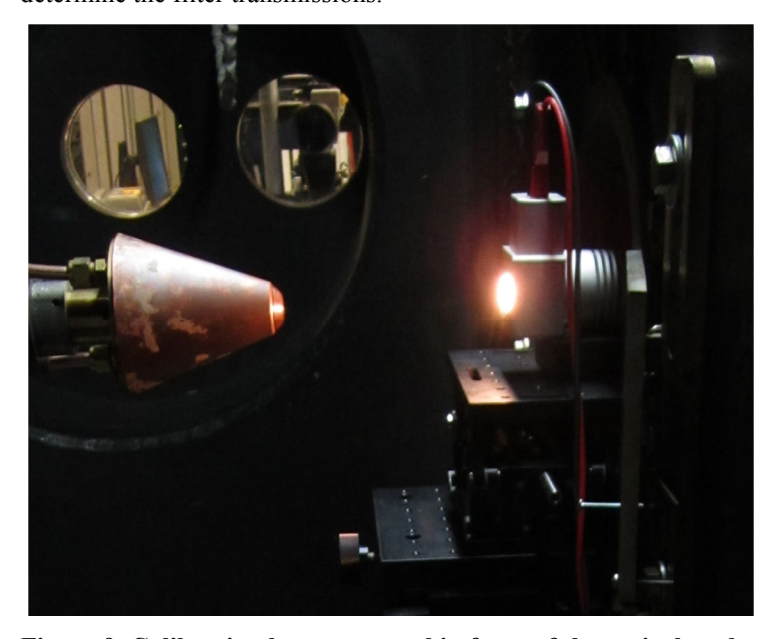


Figure 9. Calibration lamp mounted in front of the optical probe.

To increase signal to noise in the UV where the integrating sphere emission is weak, a cross calibration with a Deuterium lamp was done after completion of the test series. Although the Deuterium lamp is calibrated to spectral radiance, the magnitude depends strongly on the diameter of the measured spot. The factory calibration sheet only provides values up to 1mm measurement spot size, therefore the UV calibration factor was scaled to the one obtained from the calibration with the integrating sphere in the overlapping wavelength regions of the two lamps. Hence, a calibration down to 200 nm could be achieved. However, the combination of optical fibers, filters, and spectrometer lost its sensitivity at about 250 nm.

Since the arc-jet radiation was about 4-5 orders of magnitude higher than the light provided by the calibration lamps, significantly different acquisition times were used for arc-jet measurements (less than 1 ms) and calibration (30 s). During lab testing for the measurement campaign with the 13-inch nozzle, it became evident that the spectrometer showed a significant non-linearity with acquisition time with strong gradients for times less than 3.7ms. Therefore, different measurements with a variation of acquisition time while measuring the same radiation source were performed with three calibration lamps of different power. The result being that besides the time non-linearity the detector showed a slight decrease in sensitivity once the signal approached the saturation limit. Both non-linearities could be separated. The resulting sensitivity curves are shown in Fig. 10. All measured raw data were corrected to intensity and acquisition time sensitivity of the spectrometer before further analysis.

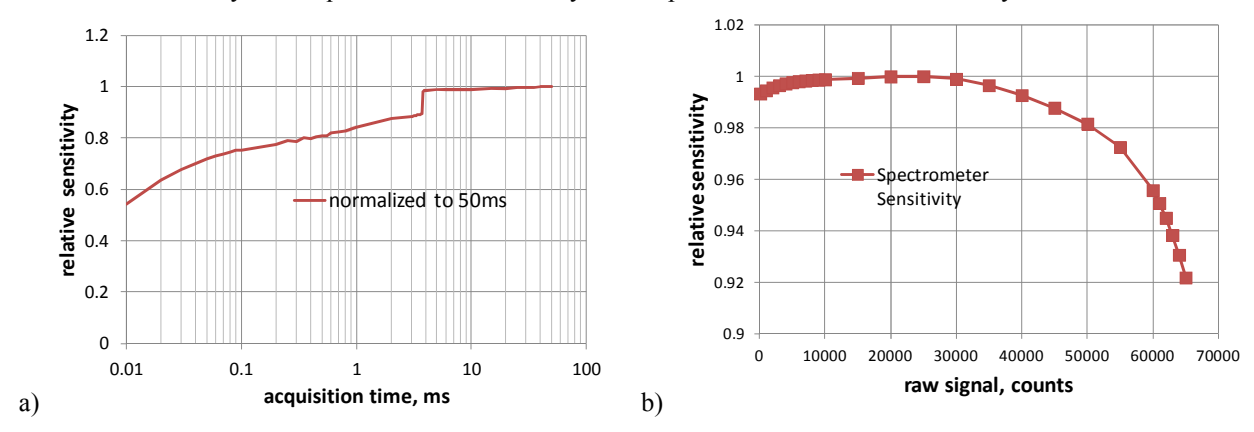


Figure 10. Relative spectrometer sensitivity vs. acquisition time (normalized to 50ms) and raw signal.

Due to the significant increase of noise level at acquisition times above several seconds, a direct measurement of the available calibration lamps including the use of neutral density filters was not possible with the Avantes spectrometer. Therefore, the calibration measurements with this spectrometer were done without neutral density filters. The filter transmission curves were separately determined with a more sensitive set-up with an Acton Sp2300 spectrometer and an Andor Newton EMCCD. Even with these more sensitive instruments, several gain and acquisition time variations had to be performed to determine EM-gain sensitivity of the used set-up and finally the filter transmission. Figure 11 shows the filter transmission for the two different neutral density filters as applied to the calibration of the arc-jet data. Both filters show a decreasing sensitivity toward lower wavelength, the T0.007 filter seems to cut off deeper in the UV. The T0.007 filter transmission was also checked during the calibration measurements inside the facility. The results were in good agreement with the lab calibration. Therefore, the T0.007 transmittance curve is considered more reliable than the ND4 one.

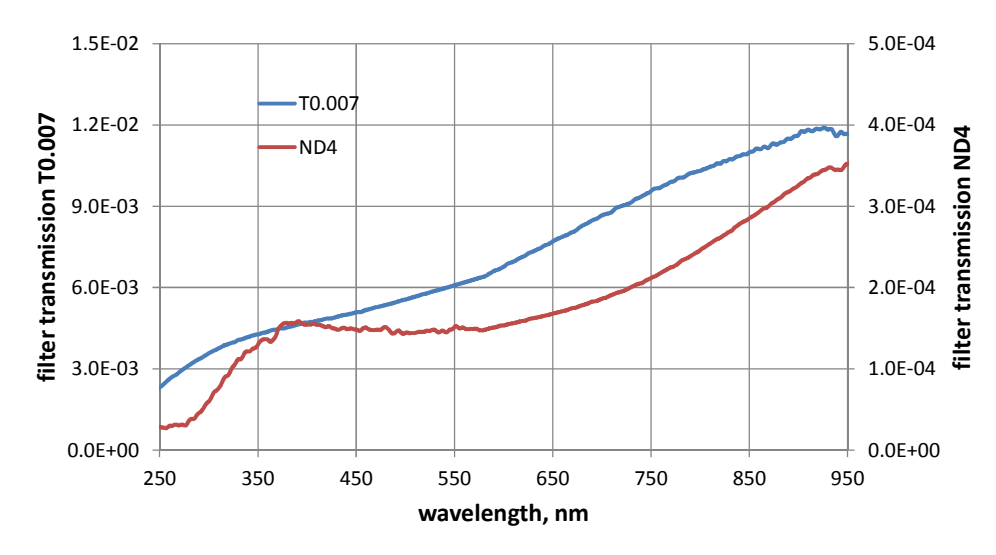


Figure 11. Filter transmissions of the neutral density filters used in the arc-jet measurements.

## **Radiometer Calibration**

For the radiometer calibration, different pinhole sizes were used in addition to the 50µm pinhole of the original arc-jet test configuration to increase the signal level. A simplified ray tracing analysis based on geometrical optics was used to determine the optical paths for the different apertures. The highest signals were expected for the integrating sphere in a distance where the radiating area was significantly larger than the measured spot size (i.e. close to the probe). Theoretically, the distance to the radiating surface should have no influence on the measured signal as long as this criterion is fulfilled. However, the effect of scattered light, e.g. from reflections inside the optical plug, are not accounted for in this scenario. Therefore, the LabSphere integrating sphere was placed in defined distances according to the ray tracing analyses to match either the case of illumination of the entire sensor area or the footprint on the sensing area during arc-jet testing.

As mentioned above, the defined receiving area in the optical path is given by the pinhole itself. Therefore, the calibration of the radiometer sensor was computed to radiant flux sensitivity. The resulting radiant flux was divided by the pinhole area to yield the incident irradiance (or radiation heat flux). Rather than using the calibration board with an amplification of ~6000, a Stanford Research Instruments low noise amplifier SR560 was used to directly measure the thermopile sensor during calibration. With this amplifier, gains of ~50000 could be reached. In parallel to the thermopile measurements, the gain of the amplifier was checked before and after the calibration by applying defined input voltages between 50 and 100  $\mu$ V. The change in amplifier gain during these measurements was below 1%. To filter ambient noise, a 0.3 Hz filter was applied during the calibration measurements. Calibration measurements were done with different pinhole sizes up to 0.85mm to increase the low signal levels of several  $\mu$ V with the 50 $\mu$ m pinhole used during arc-jet testing. Each pinhole required a different distance to the integrating sphere to catch all incoming radiation on the active sensor area. The sensitivities determined with the different pinhole sizes agreed rather well with each other, thus confirming the chosen approach. However, differences to the average value of up to  $\pm 10\%$  were observed. Figure 12 shows the obtained sensor sensitivities versus pinhole diameter.

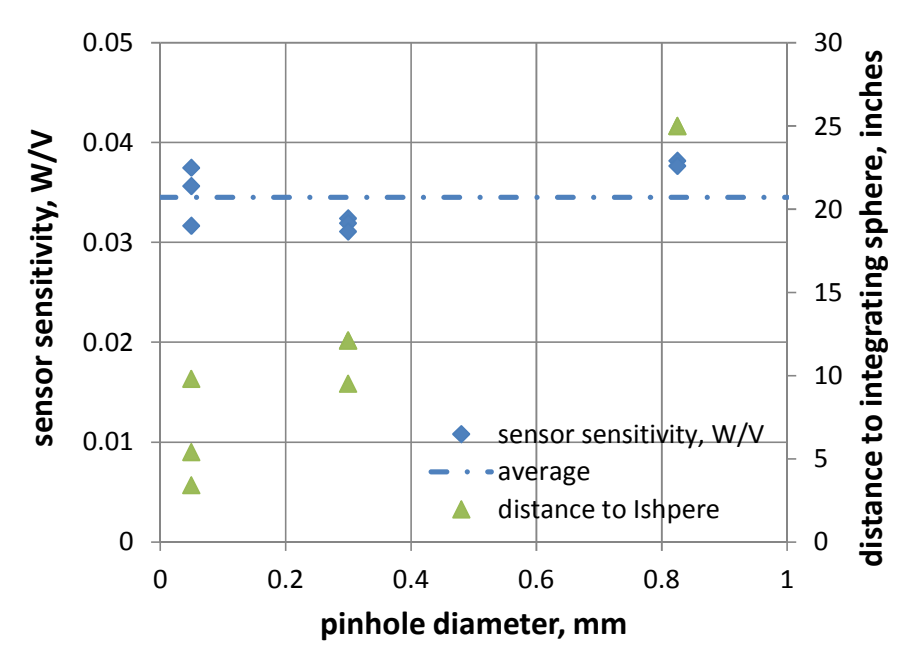


Figure 12. Measured radiometer sensitivity for different pinhole sizes.

## V. Test Conditions

For these tests, four conditions at bulk enthalpy levels between 8 and 24 MJ/kg were chosen. The conditions were chosen because there is a sizeable database of arc jet data at these conditions and flow field solutions computed with the computational fluid dynamics (CFD) code  $DPLR^{4-6}$  are readily available. Table 1 summarizes the heater settings for the test conditions. The bulk enthalpy values are determined from measured data through the EB2 method.<sup>9</sup>

Table 1: Facility Settings (first enthalpy value according to Winovich, second one EB2)

Condition	Arc Current (A)	Arc Voltage (V)	Main-Air Mass Flow Rate (g/sec)	Add-Air Mass Flow Rate (g/sec)	Argon Mass Flow Rate (g/sec)	Arc Heater Pressure (kPa)	Bulk Enthalpy (MJ/kg)
MSL-A2	3500	4330	270	330	42	486	10.6
$MSL \ 1_{mod}$	2500	3560	200	55	26	240	16.3
$(MSL1_{nominal})$	(2000)	(3700)					
Low Enthalpy	3300	6700	510	740	54	900	7.7
MSL-8	6000	7300	740	55	54	886	24.1

The conditions of Table 1 were run with the 6-inch nozzle at a probe distance to the nozzle exit plane of 3 inches. At Ames, test stream centerline conditions are routinely measured via copper slug calorimeter probes. The standard probe geometries are hemispherical (hemi), uniform heat flux (iso-q), and flat-faced. The measured heat flux depends on calorimeter shape and material properties. The heat flux on a flat-faced or an iso-q model (these two shapes are preferably used for material testing) is substantially lower than that to a hemisphere of the same base radius. Table 2 shows the measured heat flux values for the various geometries at a location of 3 inches from the exit plane of the 6-inch nozzle. Where measured values with a flat-faced or iso-q calorimeter were not available, calculated values based on the relation (2) given by Zoby and Sullivan<sup>10</sup> are shown.

$$\dot{q}_{FlatFace} = \dot{q}_{hemi} \sqrt{\frac{r_{eff,hemi}}{r_{eff,FlatFace}}} \qquad \dot{q}_{iso-q} = \dot{q}_{hemi} \sqrt{\frac{r_{eff,hemi}}{r_{eff,iso-q}}}$$
(2)

with the effective nose radiuses<sup>10</sup>:

$$r_{eff,hemi} = r_{hemi} = 2$$
 inches  
 $r_{eff,FlatFace} = 6.349$  inches  
 $r_{eff,iso-q} = 3.571$  inches

Table 2: Measured centerline heat fluxes with the 6-inch nozzle at the 3 inch location (\*computed according to Zoby and Sullivan10):

Condition	Heat flux on a 102 mm hemi calorimeter, W/cm <sup>2</sup>	Heat flux on a 102 mm iso-q calorimeter, W/cm²	Heat flux on a flat face calorimeter, W/cm <sup>2</sup>	
	Slug			
MSL-A2	1250	928 (935*)	701*	
MSL-1 mod	1008	754*	566*	
Low Enthalpy	1599	1197*	897*	
MSL-8	2074	1953 (1552*)	1164*	

## VI. Measured Spectra and Radiation Heat Fluxes

Due to the high radiation levels emitted by the arc-jet plasma, neutral density filters had to be used for the spectrometer measurements. Two different neutral density filters T.0.007 and ND4 were used for the conditions MSL-A2 and MSL-8 to provide different acquisition times. Measurements during different sweeps at the same condition gave fairly constant results. The measurements with the ND4 filter, however, yielded slightly lower radiation heat flux values than the measurements with the T0.007 filter. In Fig. 13 the spectral distribution of incident spectral irradiance (or spectral radiative heat flux) between 250 and 950nm on the IHF center-line is shown for the different IHF conditions and filters (where available).

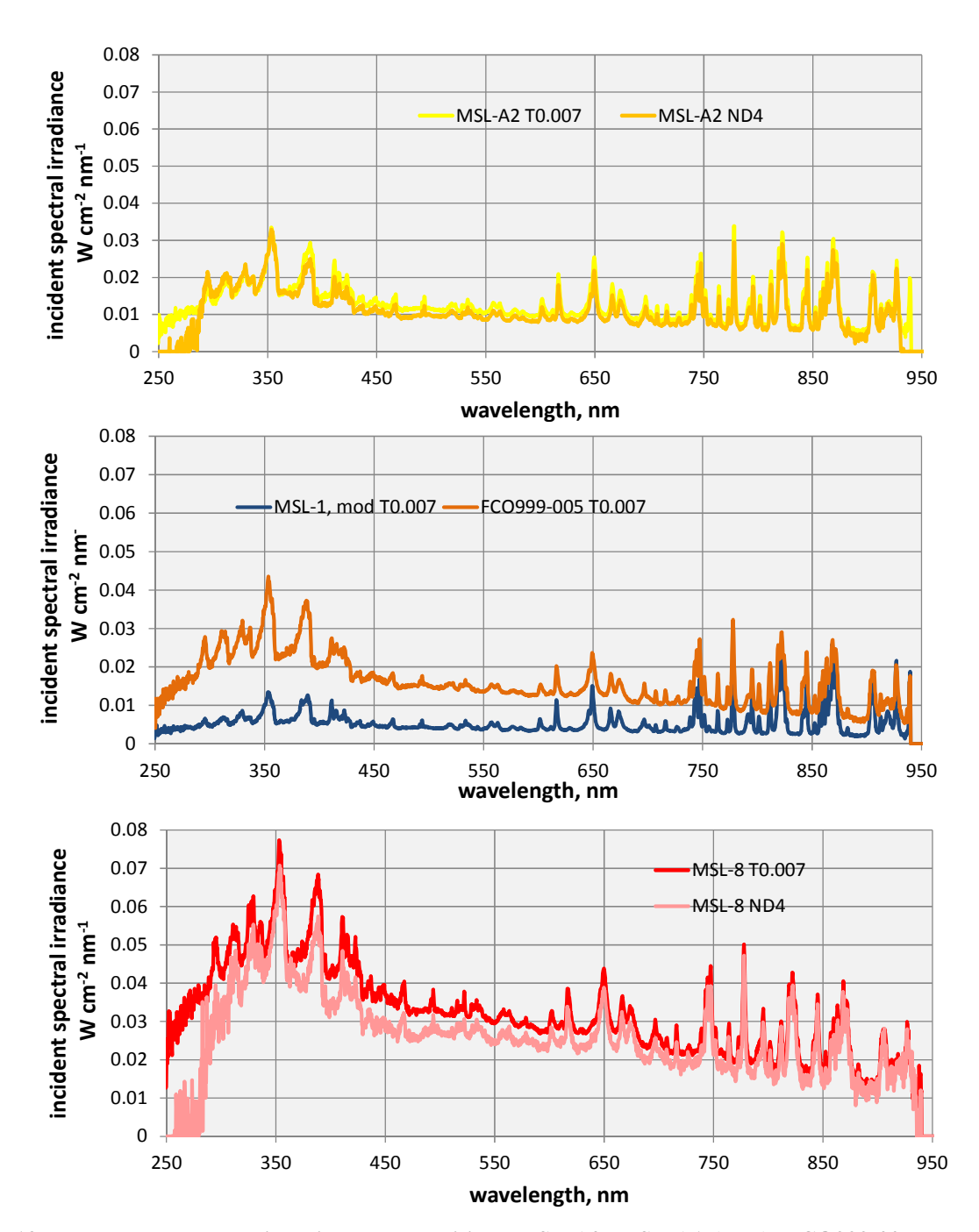


Figure 13. Measured spectral irradiance at conditions MSL-A2, MSL-A1 (mod), FCO999-005 and MSL-8 with the IHF 6-inch nozzle in a distance of 3 inches to the nozzle exit measured with the two neutral density filters (MSL-A2 and MSL-8).

As already seen in the results obtained with the 13 inch nozzle, the spectra are dominated by a strong continuum overlaid by bound-bound radiation from atomic nitrogen and oxygen and from molecular systems from  $N_2$  and  $N_2^+$ . If an arbitrary continuum is fitted to the spectra, the bound-bound radiation can be separated from the measured spectra by subtracting this continuum. The following analysis steps have been performed for the MSL-8 condition (representing the condition with the highest total and radiation heat fluxes) and the MSL-A2 condition, since for these two conditions, data with both 6-inch and 13-inch nozzles are available. The resulting continuum and bound-bound spectra for these two conditions are shown in Fig. 14.

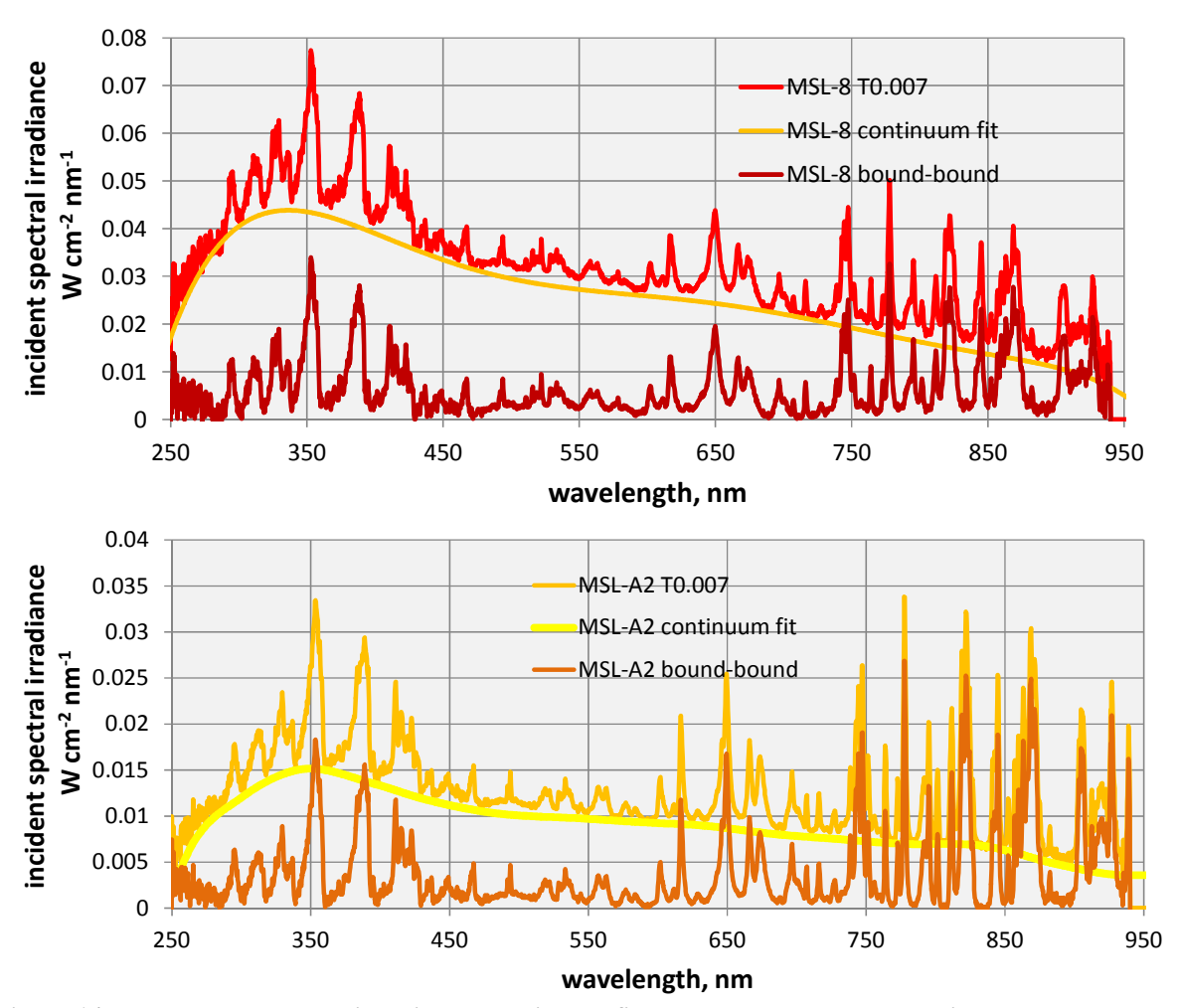


Figure 14. Measured spectral irradiance, continuum fit to these spectra, and resulting bound-bound spectra at the MSL-8 and MSL-A2 conditions.

The main bound-bound radiation at wavelengths above 600nm comes from oxygen and nitrogen atom lines. Below 500nm, the molecular bands from  $N_2$  and  $N_2^+$  in the near ultraviolet are strong emitters, NO radiation is expected to dominate below 250nm. The continuum radiation increases with lower wavelengths and peaks slightly below 350 nm. At the MSL-8 condition, 80% of the measured radiation comes from continuum emission, while at the MSL-A2 condition continuum accounts for about 76%.

Although *NEQAIR*<sup>7</sup> simulations based on flow field solutions of the flow field starting in the plenum of the archeater all the way downstream to the probe position are available, it has been shown in the analysis of the results with the 13-inch nozzle that the main radiation seen by the optical probe is generated upstream of the simulation regime.<sup>3</sup> In particular the experimentally observed continuum radiation is not present in the simulation. Rather than comparing the recent data with simulated data based on CFD simulation, a comparison to the measured data at the 13-inch nozzle location appears more meaningful.

As expected, the measured spectral irradiance shows a significant increase at the 6-inch nozzle location. The spectra are qualitatively similar as shown in Fig. 15 for the MSL-8 condition but the ratios for bound-bound and continuum radiation are different. For the MSL-8 condition, the bound-bound radiation increased by a factor of 5.25 while the continuum only increased by a factor of 2.45.

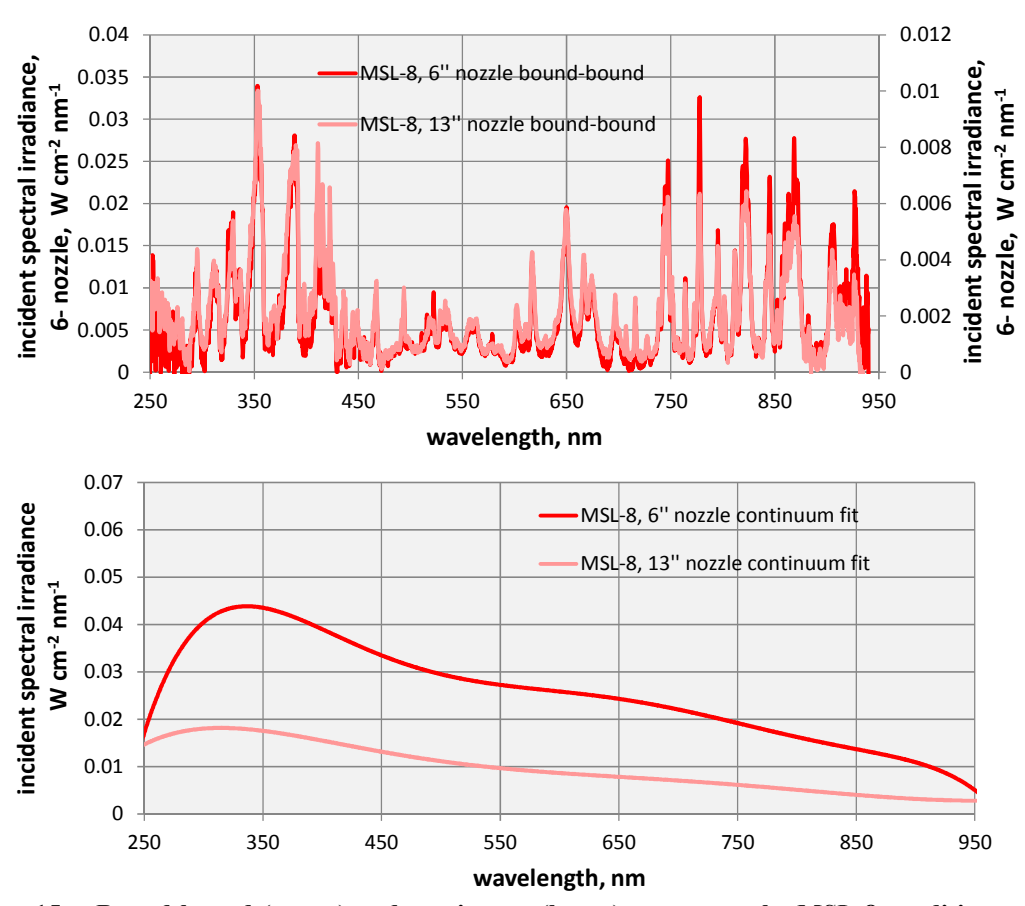


Figure 15. Bound-bound (upper) and continuum (lower) spectra at the MSL-8 condition at the 6-inch and the 13-inch nozzle test locations.

Since the internal flow field inside the arc heater does not depend on the choice of nozzle, the incident irradiance (or radiation heat flux) at the probe position only depends on geometric view factors (if the contribution of the post-shock system in front of the probe is negligible). The test location for the 6-inch nozzle is at a distance of 3 inches to the nozzle exit. The distances to the nozzle throat are 11.3 inches and 31.2 inches for the 6-inch nozzle and the 13-inch nozzle, respectively. The internal geometry of the arc-heater is the same for both nozzles. With both nozzles, the conical section of the field of view of the optical probe extends to the cathode section before the field of view is truncated by the inner wall of the heater. Therefore, the view factors for these regions are constant in both cases and a ratio of 8.3 (6-inch nozzle to 13-inch nozzle) can be calculated for the view factor. The view factors for the regions upstream from the cathode, however, approach each other with both nozzles. At a location of 50 inches (1.27m) upstream of the nozzle throat, the ratio between both nozzles decreases to 2. Figure 16 illustrates the ratio between the two view factors in the IHF internal geometry.

From the comparison of measured and simulated radiation heat fluxes at a distance of 10 inches to the 13-inch nozzle it can be concluded that more than 95% of the radiation heat flux is generated in the discharge region (i.e. from the cathode position all the way upstream through the 15 feet (~4.6m) long arc-column). If, as a zeroth-order approximation, the thermochemical state inside the arc is considered to be constant (i.e., the same amount of radiation is emitted at each axial position), the incident radiation can be estimated by an integration over the view factors along the heater axis. This very preliminary estimate of the contributions of the different arc-heater regions yields 30% radiation from the cathode region and 70% from the arc column for the 13-inch nozzle configuration. With the 6-inch nozzle, this ratio is approximately 50/50. These results yield an estimate of an increase in radiation heat flux by a factor of 3.3 by switching to a location 3 inches from the 6-inch nozzle exit. However, absorption inside the plasma is not taken into account in these considerations. Since the main gas flow is injected throughout the arc column, another assumption would be a constantly increasing plasma density between anode and cathode. Under this assumption (still without accounting for absorption) the measured radiation should increase by a factor of

3.7. If the majority of radiation is generated in the cathode region (which would be the case if the arc-column is optically thick), the factor increases up to 8, which is considered an upper bound for the radiation increase.

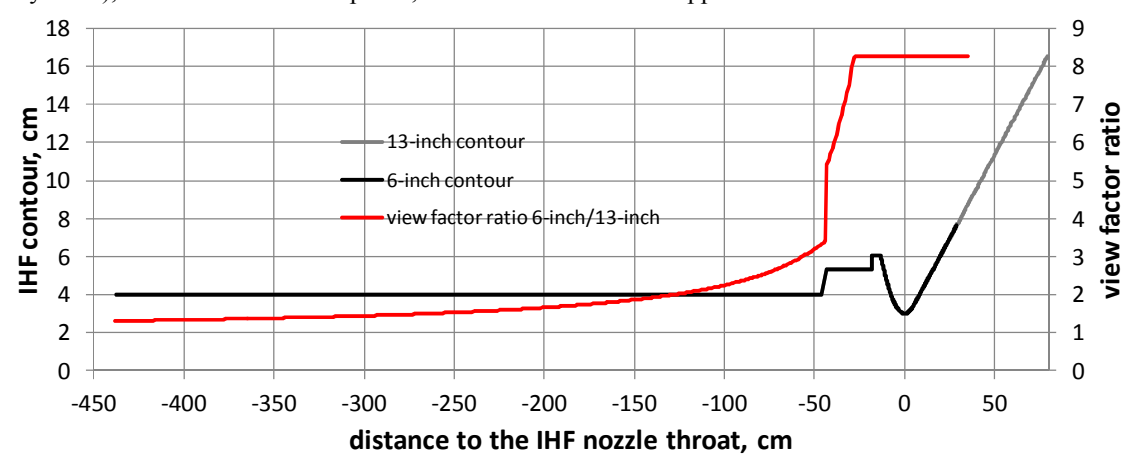


Figure 16. Ratio in view factors along the IHF axis between a test location of 10 inches distance to the 13-inch nozzle and 3 inches distance to the 6-inch nozzle for the same heater settings.

Comparing these estimates to the measured ratios at the MSL-8 condition (5.25 for bound-bound radiation, 2.45 for continuum), the majority of the measured bound-bound radiation is generated in the cathode region of the arc heater. This result is in qualitative agreement with preliminary computations of the plasma inside the arc-column showing a peak temperature decrease from about 15000K downstream of the anode to about 9000K in the cathode region. The measured continuum radiation, however, seems to be generated mainly close to the upstream electrode in the first part of the arc-column. Therefore, the arc-column seems to be at least partially optically thick for bound-bound radiation.

The same procedure applied to the measured MSL-A2 spectra yields a factor of 2.8 for the continuum and 2.3 for the bound-bound emission between the 6-inch and the 13-inch nozzle. Besides a factor of almost two in arc current, the main difference between the two conditions is the amount of add air. Room temperature air is added at this condition to drive the bulk enthalpy down while maintaining a high stagnation pressure. This procedure seems to have a substantial impact on the plasma inside the arc heater. If the arc-column distribution is considered to remain unchanged, this indicates a slight increase in continuum radiation close to the downstream electrode (e.g. by an increased amount of ion-electron recombination). The lower factor for bound-bound radiation strongly indicates a decrease of the bound-bound radiation in the cathode region (e.g. through increased absorption or decreased plasma temperature). It seems plausible to assign these processes to the added room temperature air cooling down the hot core flow. More information about the axial distribution of the plasma inside the arc heater, in particular in the cathode region, will be needed to quantify these effects.

#### **Radiation Heat Fluxes**

As already done for results with the 13-inch nozzle, radiation heat fluxes in the wavelength range from 250nm to 950nm were determined from the measured spectra by summing the emission spectra and multiplying with the corresponding wavelength increment for each pixel. Integrated over the spectral range from 250nm to 900nm, radiation heat fluxes between 6 W/cm² and 33 W/cm² are obtained for the different conditions, the individual values are plotted in Fig. 18 in comparison to the radiometer results.

In addition to these values, the thermopile radiometer measurements were analyzed to obtain total radiation heat fluxes, theoretically only limited through the sapphire window transmission which cuts off radiation below 160nm and above  $5\mu m$ . The window-less radiometer set-up was intended to eliminate even these transmission losses.

However, in the first test with the window-less configuration, the sensor failed during operation with helium while the probe was swept into the cold air flow of the IHF before electrical power was applied (i.e. no arc discharge). After disassembling the sensor, burn marks were seen in the bronze parts of the optical plug, most clearly at the pinhole facing the incoming cold stream and fainter ones at the turning points of the helium feed lines. Apparently, significant overheating inside the probe occurred while cold helium was supplied from the backside of the probe against an incoming cold gas flow. The most probable explanation so far is overheating of the helium flow through fluid dynamic oscillations, analogous to a Hartmann-Sprenger tube. 11 The current hypothesis is that the

oscillations are likely caused by a migration of the sonic point which did not stabilize on axis but oscillated in the gas feeding groove perpendicular to the optical axis. For the next test of the window-less configuration with helium feeding, the cross section after the helium feed groove was further reduced to ensure the smallest cross section and therefore the sonic transition at this point. The initial overheating phenomena were not observed with this configuration. Although thermopile signals were measured during insertion with arc-jet operation, the time shape of these signals and the variation with increasing helium flow indicated that the signals were generated through convective heating of the sensor rather than radiation heating. Pressure measurements in the feeding cavity showed a pressure increase during the sweep indicating that a supersonic expansion was not completely achieved during the sweep. Therefore, the window-less design is considered work in progress.

The radiometer with sapphire windows showed good performance. With a time constant of 10ms, insertion times between 0.5s and 1s gave a stable sensor In most cases. signal. compensating thermopile (shielded from the radiation to enable a temperature correction) showed no significant change. Figure 17 shows the typical radiometer output of both thermopiles and the final signal as the difference of both channels.

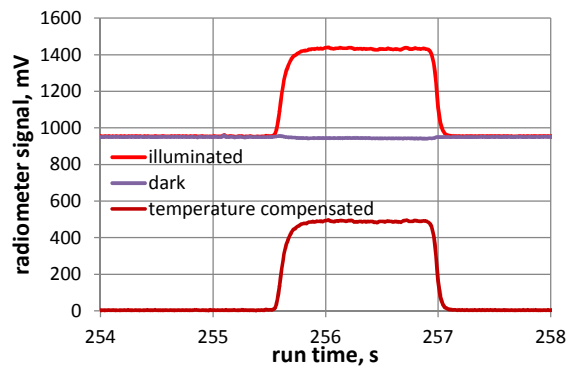


Figure 17. Typical radiometer output of both thermopiles and difference of both channels during a 1s probe insertion at the MSL-A2 condition.

The measured radiation heat fluxes account for up to 1.5% of the total heat flux to a 4-inch hemispherical calorimeter or 2.7% to a flat face which still may be considered negligible with respect to current uncertainties in measured heat flux. Figure 18 compares the radiation heat fluxes measured with the radiometer to the values from the integration over the spectrometer signals and the measured total heat fluxes to the hemispherical calorimeter.

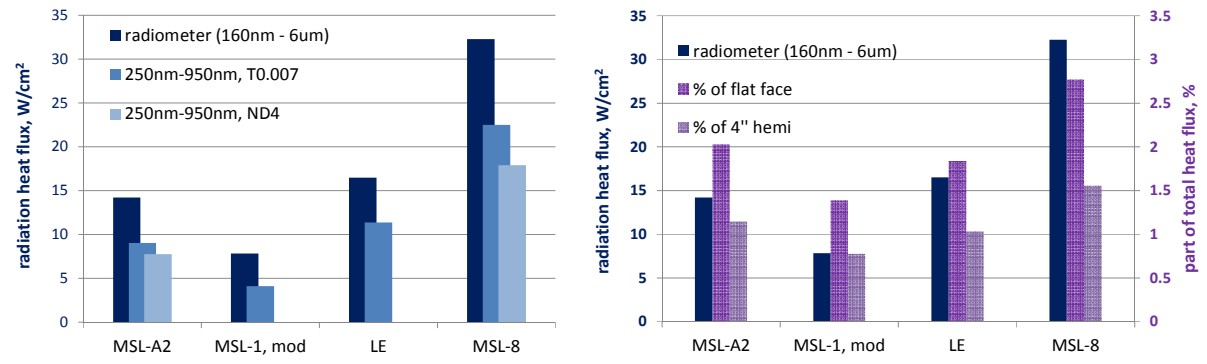


Figure 18. Radiation heat fluxes at the different IHF conditions from radiometer measurements and from spectrally integrated spectrometer signals (left) and comparison to the total heat flux measured with a 4-inch hemispherical slug calorimeter and the calculated values for a flat face one (right).

A comparison of the spectrometer and radiometer values shows that between 30% (MSL-8, highest enthalpy) to 48% (MSL-1,mod, lowest enthalpy) of the radiative heat flux is produced in the UV between 160nm and 250nm and above 950nm. From theoretical simulation for the MSL-8 condition,<sup>3</sup> about 44% of the total radiation was expected to be generated in the wavelength regions covered by the spectrometer data. The vacuum UV region below 160nm, which was not covered by these measurements, did contribute only with 1.2% of the total radiation. The larger contribution of UV-NIR radiation as seen in the measurements is attributed to the continuum radiation. However, the simulation regime was restricted to the region between plenum and probe and therefore did not include the discharge region which contributes to the total radiative heat flux with more than 95%. Additional computations of the discharge channel are in preparation and will be used for spectral simulation of the radiative heat fluxes. The measured radiation heat fluxes scale almost linearly with the applied electrical power and with the calorimeter heat flux but not with the measured bulk enthalpy as shown in Fig. 19.

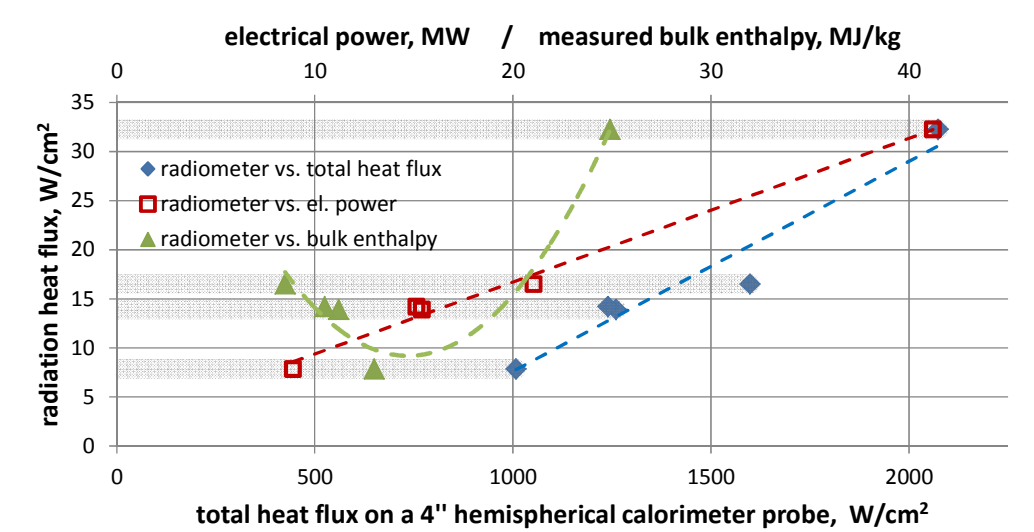


Figure 19. Radiation heat fluxes versus total measured heat flux, arc-jet input power, and measured bulk enthalpy. (Each radiation heat flux value represents one data set for a given arc-heater condition, visualized through horizontal grey bars.)

## VII. Summary and Conclusions

An optical probe was designed to measure incident radiation on a sample in the arc-jet flow as part of the heat load on a material sample in spectral resolution and with a thermopile radiometer. A fiber-coupled spectrometer was used to measure the spectral distribution of incident radiation between 250 and 950 nm.

The measured spectra were qualitatively in good agreement with those from a former measurement campaign in the 13-inch nozzle of the same facility. The spectra showed a strong continuum part, which is attributed to free-free radiation by the electrons in the discharge and free-bound continuum through ion recombination, and bound-bound spectra with major contributions form atomic oxygen and nitrogen and molecular radiation form  $N_2$  and  $N_2^+$ .

Since the heater geometry is the same for the operation with the different nozzles and the flow shows a sonic transition in the nozzle throat, the internal processes inside the heater should not be changed between operation with the different nozzles. In that case, the variation of incident radiation in the different configurations only depends on geometrical view factors. At the high condition without add air (MSL-8), the ratios between the two measurement locations indicate that the main bound-bound contribution comes from the cathode region of the arc heater. The arccolumn seems to be optically thick for bound-bound radiation to a significant amount. The continuum radiation, however, seems to be generated mainly in the upstream part of the discharge region.

For the second condition measured in both configurations, MSL-A2, both spectral components show about the same increase. If the added air is the reason for this behavior, rather complex interactions between the cold air and the hot plasma core might occur, possibly slightly increasing the emission of continuum and reducing the bound-bound radiation in the cathode and plenum region. Without further data about the axial distribution inside the arc heater more detailed explanations seem highly speculative. Future experiments could show whether this behavior is indeed related to the presence of add air in the flow.

The measured radiation heat fluxes account for up to 1.5% of the total heat flux to a 4-inch hemispherical calorimeter at the same test location or 2.7% to a flat face, increasing almost linearly with electrical arc-jet power. The radiation heat flux in the spectrometer wavelength range was determined by integrating the emission spectra which were calibrated to incident irradiance. In comparison to the total radiation measurements, between 30% (highest enthalpy condition) and 47% (lowest enthalpy condition) of the radiation heat flux comes from spectral regions outside the spectrometer range. Based on theoretical simulation, the contribution of wavelength regions not covered by the radiometer is expected to be less than 2% of the measured value. Although stronger than anticipated, the measured radiation heat fluxes are considered negligible, given typical uncertainties of the total heat flux measurements during arc-jet testing.

## Acknowledgments

The present work was supported by NASA Contract NAS2-03144 to UARC, UC Santa Cruz and NASA Contract NNA09DB39C to Jacobs Technology. The authors would like to thank Dr. David Hash (Chief, Aerothermodynamics Branch, NASA ARC) for support of modeling and simulation aspects of the present work, and wish to acknowledge the support of Jerry Ridge, Dinesh Prabhu, Michael Olsen, Mark McGlaughlin, Brett Cruden, John Balboni, Joe Hartman, Anuscheh Nawaz, Eric Noyes, Jay Grinstead, Lewis Ford, Jeffrey Mach, Roy Arakaki, Vince Meglio, and the arc jet operation crew. Critical financial support was provided by NASA-SCAP for the arc-jet operational capability at NASA Ames Research Center.

#### References

<sup>1</sup>Winter, M W, Prabhu, D K, Taunk, J S, and Terrazas-Salinas, I, "Emission Spectroscopic Measurements in the Plenum of the NASA IHF Arc Jet Facility," AIAA-2010-4522, 10<sup>th</sup> AIAA/ASME Joint Thermophysics and Heat Transfer Conference, Chicago, IL, 28 Jun - 1 Jul 2010.

<sup>2</sup>Winter M W, and Prabhu, D K, "Excited State Chemistry in the Free Stream of the NASA IHF Arc Jet Facility Observed by Emission Spectroscopy," AIAA-2011-3632, 42<sup>nd</sup> AIAA Thermophysics Conference in Honolulu, Hawaii, 27 - 30 Jun 2011.

<sup>3</sup>Michael W. Winter. Dinesh K. Prabhu, George A. Raiche, Imelda Terrazas-Salinas, and Frank C. L. Hui, Emission Spectroscopic Measurements with an Optical Probe in the NASA Ames IHF Arc Jet Facility, AIAA-2012-1016, 43<sup>rd</sup> AIAA Thermophysics Conference in Nashville, Tennessee, 9 - 12 Jan 2012.

<sup>4</sup>Wright, M J, Candler, G V, and Bose, D, "Data-Parallel Line Relaxation Method of the Navier-Stokes Equations," AIAA Journal, Vol. 36, No. 9, 1998, pp. 1603–1609.

<sup>5</sup>Wright, M.W., White, T., and Mangini, N., "Data Parallel Line Relaxation (DPLR) Code User Manual Acadia – Version 4.01.1," NASA/TM-2009-215388, October 2009.

<sup>6</sup>Prabhu, D K, et al., "CFD Analysis Framework for Arc-Heated Flowfields, I: Stagnation Testing in Arc-jets at NASA ARC," AIAA-2009-4080, 41<sup>st</sup> Thermophysics Conference, June 22-25, 2009, San Antonio, TX.

<sup>7</sup>Whiting, E E, Park, C, Liu, Y, Arnold, J O, and Paterson, J A, "NEQAIR96, Nonequilibrium and Equilibrium Radiative Transport and Spectra Program: User's Manual," NASA RP-1389, NASA, December 1996.

<sup>8</sup>Imelda, Terrazas-Salinas, J. Enrique Carballo, David M. Driver, and John Balboni, "Comparison of Heat Transfer Measurement Devices in Arc Jet Flows with Shear," AIAA 2010-5053, 10<sup>th</sup> AIAA/ASME Joint Thermophysics and Heat Transfer Conference, 28 June - 1 July 2010, Chicago, Illinois.

<sup>9</sup>Hightower, T. M., Balboni, J. A., MacDonald, C. L., Anderson, K. F., and Martinez, E. R., "Enthalpy by Energy Balance for Aerodynamic Heating Facility at NASA Ames Research Center Arc Jet Complex," 48th International Instrumentation Symposium, The Instrumentation Systems, and Automation Society, Research Triangle Park, NC, May 2002.

<sup>10</sup>Zoby, E V and Sullivan, E M, "Effects of Corner Radius on Stagnation-Point Velocity Gradients on Blunt Axisymmetric Bodies." NASA TMX-1067, NASA, January 1966.

<sup>11</sup>Brocher, Eric, "On The Maximum Attainable Temperature in Hartmann-Sprenger Tubes," In: Shock tubes and waves; Proceedings of the Twelfth International Symposium, Jerusalem, Israel, July 16-19, 1979. (A80-38078 15-34) Jerusalem, Magnes Press, 1980, p. 161-168.